



Impact of variations of gravitational acceleration on the general circulation of the planetary atmosphere



Cevahir Kilic^{a,b,*}, Christoph C. Raible^{a,b,c}, Thomas F. Stocker^{a,b,c}, Edilbert Kirk^d

^a Center for Space and Habitability, University of Bern, Sidlerstrasse 5, CH-3012, Bern, Switzerland

^b Climate and Environmental Physics, Physics Institute, University of Bern, Sidlerstrasse 5, CH-3012, Bern, Switzerland

^c Oeschger Centre for Climate Change Research, University of Bern, Falkenplatz 16, CH-3012, Bern, Switzerland

^d Meteorological Institute, University of Hamburg, Bundesstrasse 55, 20146, Hamburg, Germany

ARTICLE INFO

Keywords:

Planetary atmospheres
General atmospheric circulation
Global energy cycle
Gravitational acceleration
Atmospheric simulation

ABSTRACT

Fundamental to the redistribution of energy in a planetary atmosphere is the general circulation and its meridional structure. We use a general circulation model of the atmosphere in an aquaplanet configuration with prescribed sea surface temperature and investigate the influence of the gravitational acceleration g on the structure of the circulation. For $g = g_0 = 9.81 \text{ m s}^{-2}$, three meridional cells exist in each hemisphere. Up to about $g/g_0 = 1.4$ all cells increase in strength. Further increasing this ratio results in a weakening of the thermally indirect cell, such that a two- and finally a one-cell structure of the meridional circulation develops in each hemisphere. This transition is explained by the primary driver of the thermally direct Hadley cell: the diabatic heating at the equator which is proportional to g . The analysis of the energetics of the atmospheric circulation based on the Lorenz energy cycle supports this finding. For Earth-like gravitational accelerations transient eddies are primarily responsible for the meridional heat flux. For large gravitational accelerations, the direct zonal mean conversion of energy dominates the meridional heat flux.

1. Introduction

Since the discovery of the first giant planet outside of our Solar System in 1995 (Mayor and Queloz, 1995) methods to detect and characterise new planets have been continually developed (e.g. Malbet et al., 2012). Physical parameters of exoplanets such as angular velocity, size and mass, can now be estimated and the composition of an atmosphere can be constrained (e.g. Deming et al., 2005; Berta et al., 2012; Kreidberg et al., 2014). The increasing number of newly detected planets and their characteristics raises questions on whether other habitable worlds might exist.

Apart from the Earth, Venus, Mars, and Titan are planets or moons with substantial atmospheres (e.g. Svedhem et al., 2007; Lewis et al., 1999). The corresponding atmospheric circulations differ from each other due to different characteristics and physical parameters of the planets and moons, such as the atmospheric composition, distance to the star, angular velocity, size, obliquity, and composition of the planetary body - the latter determining the gravitational acceleration at the surface. The atmospheric circulation is the primary process to transport heat meridionally; therefore, planetary habitability is directly dependent on this parameter.

The purpose of this study is to investigate the effect of changes in

the gravitational acceleration on the atmospheric dynamics associated with the general circulation. We employ a three-dimensional atmospheric general circulation model (GCM) of intermediate complexity in an aquaplanet configuration (Lunkeit et al., 2011). A set of sensitivity simulations is performed varying only the gravitational acceleration and keeping the atmospheric mass constant. The analysis focuses on the meridional circulation and the different drivers. The consideration of the energy budget based on Lorenz (1955) provides a deeper understanding of the atmospheric conditions of an exoplanet, a prerequisite to assess habitability.

On Earth, the meridional energy imbalance between equator and poles induces a heat transport that is essential for the formation of the atmospheric circulation (e.g. Holton, 2004). The meridional circulation consists of a three-cell structure: a thermally direct Hadley cell, a thermally indirect Ferrel cell, and a thermally direct polar cell in each hemisphere. Quantification of the strength of the individual drivers of these cells provides an understanding of the sensitivity of the meridional circulation to changes in external parameters such as the gravitational acceleration. For the thermally direct Hadley cell, the diabatic and latent heating are essential, while for the thermally indirect Ferrel cell the eddy momentum and heat fluxes are the dominant drivers (e.g. Holton, 2004). The zonal drag force balances the resulting zonal component of Hadley

* Corresponding author at: Center for Space and Habitability, University of Bern, Sidlerstrasse 5, CH-3012, Bern, Switzerland.
E-mail address: kilic@climate.unibe.ch (C. Kilic).

circulation and the eddy momentum flux of the Ferrel cell.

The energy cycle as presented by Lorenz (1955) considers different forms of energy in the atmosphere, the associated transfer fluxes, and sources and sinks of energy on a global scale. On Earth, available potential energy is generated by diabatic and latent heating, then converted into kinetic energy and finally dissipated by friction and turbulence. The circulation is separated into three components: zonal mean flow, transient eddies and stationary eddies (Peixoto and Oort, 1992). Stationary eddies are caused by zonal asymmetries primarily due to land-sea distribution and orography. On an aquaplanet, stationary eddies were found to be negligible (Manabe and Terpstra, 1974; Grose and Hoskins, 1979; Held et al., 1983).

Early attempts to assess the atmospheric dynamics in particular the meridional circulation were made by Held and Hou (1980). They qualitatively estimated the width of the thermally direct cell for different terrestrial planets from basic principles. Caballero et al. (2008) further developed the findings of Held and Hou (1980) and introduced a semi-analytical theory for the depth, width and strength of the thermally direct cell, which are in good agreement with GCM simulations of Mars and Snowball Earth.

The dependence of the thermally driven flow under various rotation frequencies (e.g. Williams and Holloway, 1982; Williams, 1988a, 1988b; Read, 2011; Kaspi and Showman, 2015; Chemke and Kaspi, 2015 and references therein), and for tidally locked configurations (e.g. Joshi et al., 1997; Joshi, 2003; Merlis and Schneider, 2010) were investigated using GCMs. For a slowly rotating planet, the meridional atmospheric circulation consists of just one thermally direct cell, which extends from the equator to the pole and maintains the meridional heat flux. In the Northern Hemisphere, the increase of the angular velocity leads to a deflection of poleward (equatorward) moving air to the East (West) in the upper (lower) troposphere due to the Coriolis acceleration. The faster the planet rotates, the more important baroclinic eddies become for the meridional heat transport in the mid-latitudes. The thermally direct cell gradually weakens, and a three-cell structure develops, similar to that observed on the Earth. However, for rotation rates larger than the one on Earth, the baroclinic eddies become less efficient, since eddy length scales become small.

Other studies have investigated the impact of size and gravitational acceleration on the atmospheric circulation and temperature distribution (Heng and Vogt, 2011; Kaspi and Showman, 2015). The latter investigated the dependence of the meridional heat flux on a set of basic parameters including atmospheric mass and gravitational acceleration for an aquaplanet configuration. Increasing the atmospheric mass, they found a weakening of the subtropical jet and an intensification of the meridional circulation in response to increasing mass. For larger gravitational accelerations with fixed atmospheric mass, they showed an intensification of the meridional circulation which was in agreement with a growth of eddy energy and an increase of equator-to-pole temperature difference, while the three-cell pattern of the meridional circulation remained unchanged. Here we also explore the atmospheric circulation of potential habitable planets with mean densities at the upper physical limit and focus on underlying mechanisms, an approach missing in earlier studies.

The outline of the study is as follows: Section 2 introduces the model setup, the experimental design, and the analysis methods. In Section 3, the reference and the sensitivity experiments are described, focusing on the meridional circulation and the underlying mechanisms. The energy budget of the reference experiment is compared to the sensitivity experiments in Section 4. Finally, we provide a discussion and concluding remarks in Section 5.

2. Experimental design and methods

2.1. Model

We use the Planet Simulator developed by the Meteorological

Institute of the University of Hamburg, Germany (Lunkeit et al., 2011). The spatial fields are represented on a spectral grid T42 which corresponds to a resolution of about $2.8^\circ \times 2.8^\circ$. The model uses 10 sigma levels up to the tropopause (100 hPa for Earth-like conditions). This is a relatively coarse vertical resolution making this a model of reduced complexity.

The dynamical core of the atmospheric model is based on the dimensionless primitive equations (Hoskins and Simmons, 1975). They include the hydrostatic approximation and the conservation of mass, heat, and momentum (Lunkeit et al., 2011).

The shortwave radiation scheme distinguishes between clear (Lacis and Hansen, 1974) and cloudy sky (Stephens, 1978; Stephens et al., 1984). The longwave radiation for the clear sky is described by a broadband emissivity method (e.g. Manabe and Möller, 1961; Boer et al., 1984). Longwave radiation of clouds is approximated as a grey body depending on the cloud liquid water content.

Furthermore, a Kuo-type convection scheme is used (Kuo, 1965, 1974). The horizontal diffusion parameterisation is based on the approach of Laursen and Eliassen (1989). The vertical diffusion, representing the non-resolved turbulent exchange, is applied to the horizontal wind, the potential temperature, and the specific humidity. The turbulent fluxes of zonal and meridional momentum, heat, and moisture are parametrised by linear diffusion along the vertical gradient with exchange coefficients for momentum and heat. Thus, the parameterisation follows the mixing length approach as an extension of the similarity theory used to define the drag and transfer coefficients (Lunkeit et al., 2011; Roeckner et al., 1992). The model includes a seasonal cycle.

2.2. Experimental setup and reference simulation

For the simulations, we use an aquaplanet configuration, which is initialised with no sea ice cover. Further, Earth-like parameters are used, i.e., the radius is 6371 km, obliquity is 23.4° , and angular velocity is $7.29 \cdot 10^{-5} \text{ s}^{-1}$. The solar constant is set to 1365 W m^{-2} and the CO_2 concentration to 360 ppm. The roughness length at the surface is $1.5 \cdot 10^{-5} \text{ m}$. The surface background albedo for open water is 0.069. The experiments use zonally uniform, prescribed sea surface temperatures (SST) following the approach of Neale and Hoskins (2000):

$$T_s(\varphi) = \begin{cases} T_0 + (T_{max} - T_0)(1 - \sin^2 \frac{3\varphi}{2}), & \text{if } |\varphi| < \frac{\pi}{3}, \\ T_0, & \text{otherwise} \end{cases} \quad (1)$$

where φ is the latitude, $T_{max} = 27^\circ \text{C}$, and $T_0 = 0^\circ \text{C}$. Thus, SSTs are constant in time representing an ocean with infinite heat capacity.

For the reference simulation the gravitational acceleration is set to $g = \tilde{g} \times g_0$ with $g_0 = 9.81 \text{ m s}^{-2}$. The atmospheric dynamics on an aquaplanet differ in some important aspects from those on Earth. The atmospheric circulation is nearly symmetric about the equator as the only source for interhemispheric asymmetry are the planetary obliquity of 23.4° and the orbital eccentricity. Fig. 1 shows the 10-year means of the zonal mean temperature and the zonal-mean zonal wind field for $\tilde{g} = 1$. As an aquaplanet has no orography, the zonal wind is generally stronger than on Earth. The lack of orography also implies that stationary eddies are almost absent and, thus, the transport of heat and momentum is dominated by transient eddies (Peixoto and Oort, 1992). Nevertheless, quasi-stationary eddies (up to one month) exist in the reference similar but much weaker and less persistent than in earlier studies (Watanabe, 2005; Zappa et al., 2011).

For the sensitivity experiments, \tilde{g} varies between $\frac{1}{4}$ and 5. Realistic values of \tilde{g} range from 0.4 (MgSiO_3 , H_2O) to 2.56 (Fe) for an Earth-sized planet (Seager et al., 2007). Pure water/ice planets would have even smaller \tilde{g} (Dressing et al., 2015). The surface pressure is adjusted when changing \tilde{g} so that the atmospheric mass remains constant. All simulations are carried out for 40 model years; typically a steady-state of the atmosphere is reached after 4–10 years.

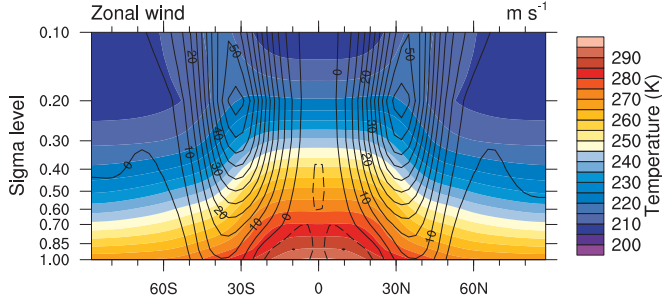


Fig. 1. The zonal-mean zonal wind (contours, interval: 5 m s^{-1}) and temperature (colours, unit: K) is shown as a climatological annual mean. The zonal wind field contour goes from -8 to 52 m s^{-1} by 4 m s^{-1} , where negative contours are dashed and zero contours are thick lines.

2.3. Methods

To analyse circulation patterns, we use climatological annual means based on 12-h model output of the last 10 model years. This selection guarantees that artificial drifts from the initialisation are excluded from the analysis. In addition to time means, zonal means and their corresponding deviations are used (for notation see Appendix A).

To understand the atmospheric circulation, we consider the zonally averaged velocity component $[v]$ and introduce the meridional mass stream function

$$\Psi(\varphi, p, t) = \frac{2\pi a \cos \varphi}{g} \int_p^{p_s} [v(\varphi, p, t)] dp, \quad (2)$$

where p is the pressure, p_s the surface pressure, a the planetary radius, g the gravitational acceleration, and φ the latitude. Furthermore, we describe the meridional heat transport by using the moist static energy (MSE) flux:

$$\overline{m} = \overline{v} \overline{m} + \overline{v' m'} = c_p T + gz + L_e q, \quad (3)$$

where $c_p = 1004 \text{ J kg}^{-1} \text{ K}^{-1}$ is the specific heat capacity of dry air, $L_e = 2.5 \cdot 10^6 \text{ J kg}^{-1}$ the latent heat of vaporisation, T the temperature, z the height, and q the specific humidity.

To quantify the drivers of the meridional circulation, we apply a β -plane approximation in Cartesian coordinates to the meridional mass stream function with $[\chi(y, z, t)] \approx \frac{\Psi(\varphi, p, t)}{2\pi a \cos \varphi}$:

$$\rho_0 \cdot [v] = - \frac{\partial [\chi]}{\partial z} \quad \rho_0 \cdot [w] = \frac{\partial [\chi]}{\partial y}, \quad (4)$$

where w is the vertical wind component and $\rho_0(z)$ is the air density. The stream function $\chi(y, z, t)$ satisfies the following partial differential equation as derived by Holton (2004) (see Appendix B):

$$\frac{N^2}{\rho_0} \cdot \frac{\partial^2 [\chi]}{\partial y^2} + f^2 \cdot \frac{\partial}{\partial z} \left(\frac{1}{\rho_0} \cdot \frac{\partial [\chi]}{\partial z} \right) = \frac{\kappa}{H} \cdot \frac{\partial [J]}{\partial y} - \frac{R}{H} \cdot \frac{\partial^2 [v^* T^*]}{\partial y^2} - f \cdot \frac{\partial^2 [u^* v^*]}{\partial z \partial y} + f \cdot \frac{\partial [X]}{\partial z}. \quad (5)$$

Besides the β -plane approximation, this partial differential equation is derived from the quasi-geostrophic equations for dry air, using the hydrostatic approximation and the thermodynamic energy equation. The four terms on the right hand-side indicate the drivers of the meridional circulation: diabatic heating, eddy heat and momentum fluxes, and zonal drag force. Note that the effects of latent heating are ignored in Eq. (5); see Appendix B. The variable H is the standard scale height given by

$$H = \frac{R \cdot T_s}{g}, \quad (6)$$

which is the maximum height over which eddies caused by baroclinic instability transport heat (Held, 1978). In log-pressure coordinates, the vertical coordinate is defined as

$$z = -H \cdot \ln \left(\frac{p}{p_s} \right) \quad (7)$$

and the density profile is given as

$$\rho_0(z) = \rho_s \cdot \exp \left(-\frac{z}{H} \right), \quad (8)$$

where ρ_s is the air density at the surface. Further, N is the Brunt-Väisälä frequency given by

$$N^2 = \frac{R}{H} \cdot \left(\kappa \cdot \frac{dT}{dz} + \frac{d(T)}{dz} \right), \quad (9)$$

where R denotes the gas constant of dry air and $\kappa = \frac{R}{c_p}$. $J(y, z)$ is the diabatic heating rate

$$[J] = c_p \cdot \left(\frac{\partial [T]}{\partial t} + \frac{N^2 \cdot H}{R} \cdot [w] + \frac{\partial [v^* T^*]}{\partial y} \right). \quad (10)$$

$X(y, z)$, the zonal drag force, is the mean shear in the zonal direction

$$[X] = \frac{\partial [u]}{\partial t} - f \cdot [v] + \frac{\partial [u^* v^*]}{\partial y}. \quad (11)$$

Note that stationary eddies are negligible due to the absence of orography. Hence, the zonal and time mean of eddy heat and momentum fluxes can be approximated by $[\overline{v^* T^*}] \approx [\overline{v' T'}]$ and $[\overline{u^* v^*}] \approx [\overline{u' v'}]$ (Appendix C) in Eqs. (5), (10) and (11). Further, the tendencies of temperature in Eq. (10) and of the zonal wind in Eq. (11) are negligible for 10-year annual means.

The numerical solution of the β -plane approximation of the mass stream function $[\chi]$ underestimates the strength compared to Eq. (2) because latent heating is not taken into account (Appendix B). However, the structure of the cell is well captured.

The solution of Eq. (5) can be represented by an appropriate double Fourier series in y and z which satisfies the boundary conditions. In this case, the left-hand side of Eq. (5) is proportional to $-[\chi]$, and for a qualitative discussion Holton (2004) suggests

$$[\chi] \propto - \frac{\partial}{\partial y} (\text{diabatic heat sources}) + \frac{\partial^2}{\partial y^2} (\text{eddy heat flux}) + \frac{\partial^2}{\partial z \partial y} (\text{eddy momentum flux}) - \frac{\partial}{\partial z} (\text{zonal drag force}). \quad (12)$$

For a more comprehensive understanding, we also examine the Lorenz energy cycle (Appendix D) of the general circulation (Section 4).

3. Influence of \tilde{g} on the general atmospheric circulation

To assess the impact of variations of \tilde{g} on the general atmospheric circulation, we investigate the zonal mean meridional circulation and its drivers using Eq. (5). We consider the reference simulation ($\tilde{g} = 1$) and compare it with the sensitivity simulations for $\tilde{g} = 0.5$ and 3.

3.1. General circulation and meridional temperature distribution

For the reference simulation $\tilde{g} = 1$, the meridional circulation consists of a three-cell structure in both hemispheres, with thermally direct Hadley and polar cells and a thermally indirect Ferrel cell in between (Fig. 2). The meridional circulation for $\tilde{g} = 0.5$ retains the three-cell structure but is weaker in strength. For $\tilde{g} = 3$ the Hadley cell merges with the polar cell, and a very weak Ferrel cell survives in the lower layers of the atmosphere.

We now examine the relation between \tilde{g} and the strength of the cells in the Northern Hemisphere. As indicators we consider the maximum (minimum) of \overline{V} for the Hadley (Ferrel) cell, and the maximum of \overline{V} for $\varphi > 55^\circ \text{N}$ for the polar cell.

Our extensive sensitivity experiments show that the thermally direct Hadley cell strengthens linearly with increasing \tilde{g} (Fig. 3a). The Ferrel

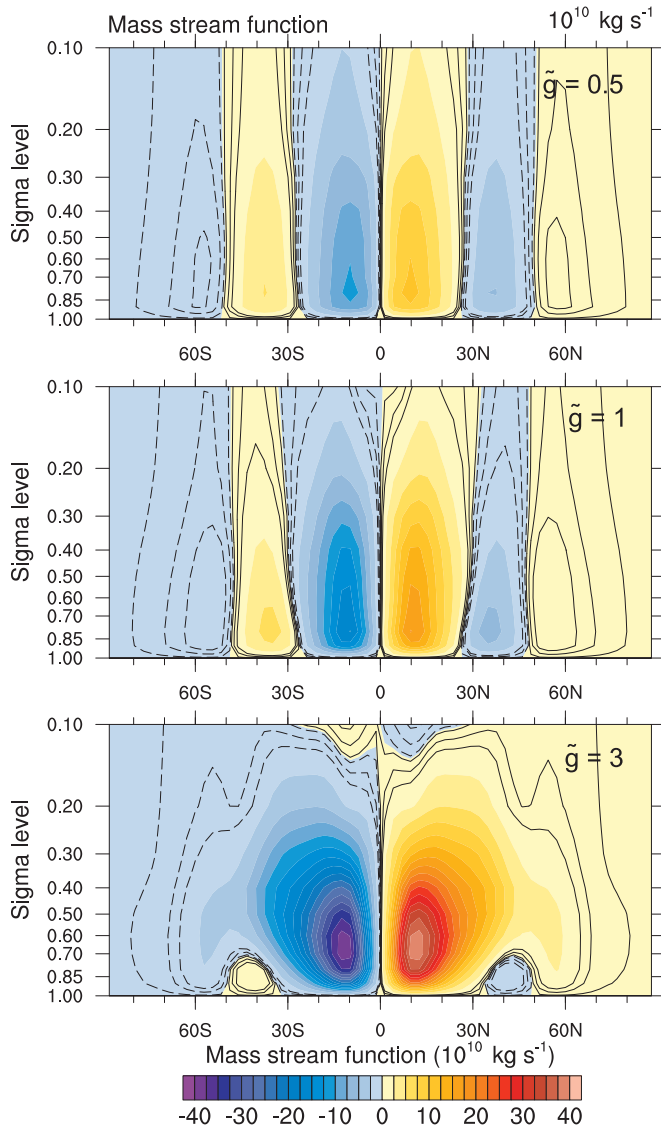


Fig. 2. Mass stream function shown with colours (interval: $2.5 \cdot 10^{10} \text{ kg s}^{-1}$) and, for better visibility, contour lines (for $\pm 0.1 \cdot 10^{10}$, $\pm 0.5 \cdot 10^{10}$, and $\pm 1 \cdot 10^{10} \text{ kg s}^{-1}$). Shown are the annual means over 10 years for $\tilde{g} = 0.5, 1, \text{ and } 3$.

cell shows a different behaviour: Its absolute strength also increases, then levels off around $\tilde{g} \approx 1.2\text{--}1.4$ and decreases (Fig. 3b). For $\tilde{g} > 2.4$, the intensity of the Ferrel cell decreases rapidly and vanishes toward $\tilde{g} = 4$. For $\tilde{g} = 0.25\text{--}2.6$, the strength of the Polar cell also exhibits a linear increase and eventually merges with the Hadley cell to form a one-cell circulation (Fig. 3c).

The increase of \tilde{g} also changes the zonal mean temperature (Fig. 4). With stronger \tilde{g} the polar areas become colder, while the upper troposphere warms. To assess these changes, we analyse the MSE fluxes decomposed in eddy and time mean part. For $\tilde{g} \leq 1.4$, the eddy contribution of the poleward MSE flux increases, while for larger \tilde{g} its contribution decreases (Fig. 5a). The mean MSE energy flux becomes the dominating contribution for large \tilde{g} (Fig. 5b, c). The total MSE flux increases with \tilde{g} only up to the mid-latitudes where the subtropical jet deflects the warm air eastward (Fig. 4 for $\tilde{g} = 3$). Hence, the cooler polar areas that are found for $\tilde{g} = 3$ are not related to the atmospheric circulation changes.

Still, the change in temperature influences the zonal wind field and vice versa. The thermal wind balance is a good approximation to explore the sensitivity of the eastward jet to changes in the thermal structure of the atmosphere:

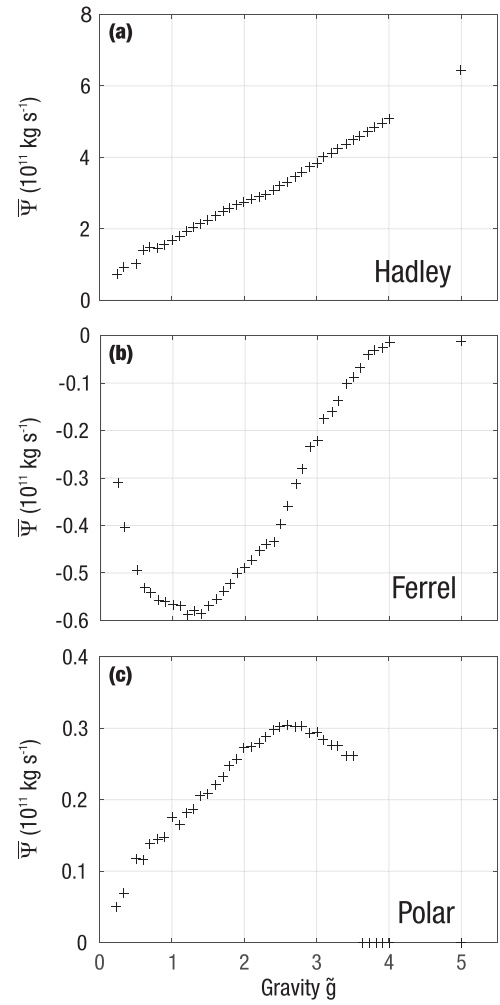


Fig. 3. The intensity of the mass stream function $\bar{\Psi}$ for (a) the Hadley cell, (b) the Ferrel cell, and (c) the polar cell in the Northern Hemisphere.

$$p \frac{\partial u_g}{\partial p} = \frac{R}{f} \frac{\partial T}{\partial y}, \quad (13)$$

where u_g is the geostrophic zonal wind. The right hand side of Eq. (13) is plotted in Fig. 6. The minimum of $\frac{\partial T}{\partial y}$ occurs around 30° latitude coincident with the location of the subtropical jet. Both in the case of $\tilde{g} = 0.5$ and $\tilde{g} = 3$, the absolute value of this minimum is smaller than in the case of $\tilde{g} = 1$; this is also true for the intensity of the subtropical jet. The latitude of the subtropical jet remains unchanged between the experiments at the level $\sigma = 0.2$ and $32\text{--}35^\circ$ latitude (one horizontal grid point difference), where $\frac{\partial T}{\partial y}$ changes sign. The width of the subtropical jet stream extends poleward when \tilde{g} increases, because the poles become cooler and the equator warms (Fig. 4). This implies an increase of the horizontal temperature gradient at mid- and high-latitudes (Fig. 6) which results in a stronger zonal wind in these regions.

Fig. 7a shows the climatological annual mean of the maximum zonal-mean zonal wind $[\bar{u}_{max}]$ as a function of \tilde{g} . $[\bar{u}_{max}]$ increases with increasing \tilde{g} , levels off at $\tilde{g} \approx 1.4\text{--}1.5$, and decreases for large \tilde{g} . This behaviour is similar to the intensity of the Ferrel cell (Fig. 3b).

Changes of the meridional circulation correspond to changes in the meridional wind. To illustrate this, the maximum $[\bar{v}_{max}]$ (poleward flow) and minimum $[\bar{v}_{min}]$ (equatorward flow) in Northern Hemisphere are shown in Fig. 7b as a function of \tilde{g} . $[\bar{v}_{max}]$ increases approximately linearly with \tilde{g} , similar to the Hadley cell intensity (Fig. 3a). The absolute value of $[\bar{v}_{min}]$ also increases with growing \tilde{g} , where the increase becomes smaller with stronger \tilde{g} . The reason for this non-linear behaviour is that the drag force near the surface increases with

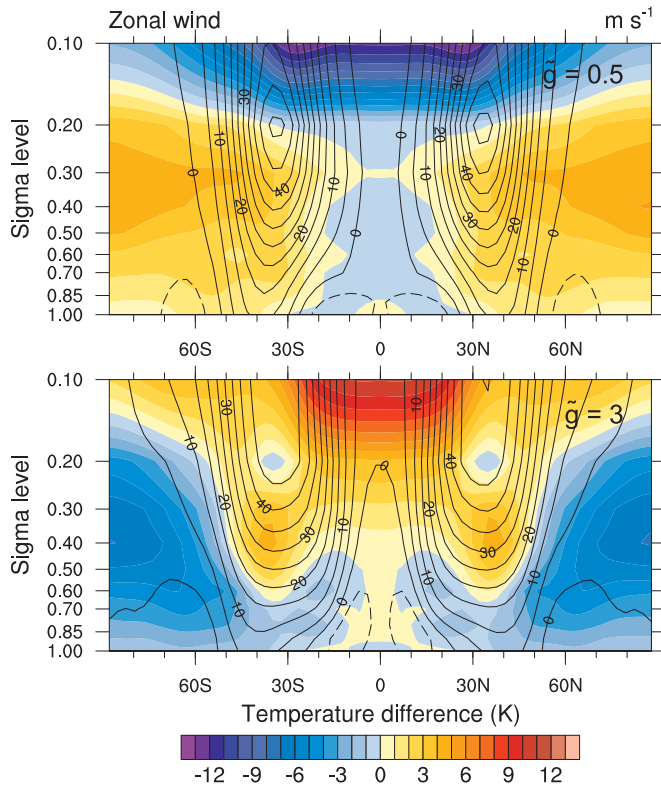


Fig. 4. Colours indicate temperature differences (experiment minus reference simulation; unit: K) and contours represent zonal-mean zonal winds (interval: 5 m s^{-1}) for $\tilde{g} = 0.5$ and 3. Shown are the climatological annual means using 10 years.

increasing wind speed.

3.2. Drivers of the meridional circulation

We now examine the specific drivers of the meridional circulation using Eq. (5) for $\tilde{g} = 0.5$ and $\tilde{g} = 3$ and compare them to the reference simulation $\tilde{g} = 1$.

An important driver is the diabatic heating rate J related to radiative heating in the dry model of Holton (2004). In our model the effect of the latent heating rate ($\frac{dL}{dt}$) is also included (Fig. 8a). This driver is significant but limited to the tropics and the low-level subtropics. Importantly, the pattern is qualitatively similar to J . For the reference simulation $\tilde{g} = 1$, J dominates between 30°S and 30°N . This is the main driver of the thermally direct Hadley cell.

The thermally indirect Ferrel cell is driven primarily by the eddy heat flux (Fig. 8c) and eddy momentum flux (Fig. 8d) but with important contributions from the zonal drag force. For the reference simulation $\tilde{g} = 1$, around $30\text{--}60^\circ$ latitude, the eddy heat flux $[\overline{v^*T^*}]$ (Fig. 8b) transfers heat poleward due to transient synoptic-scale eddies. The eddy momentum flux $[\overline{u^*v^*}]$ for $\tilde{g} = 1$ has a maximum at about 30° latitude in the Northern Hemisphere. Fig. 8e shows the zonal drag force in the zonal direction according to Eq. (11) which acts to dissipate convergence of eddy momentum flux.

For a qualitative discussion of how the four drivers contribute to the circulation, we consider Eqs. (5) and (12), and show in Fig. 9 the four terms of Eq. (12) in latitude-height sections. For the reference simulation, the diabatic heating term dominates at the equator (Fig. 9a). At mid-latitudes all forcing terms have an effect; however, it is primarily a combination of the eddy terms that lead to an enhancement of the Ferrel cell (Fig. 9b, c). The contribution of the zonal drag force forcing term causes a weakening of the Ferrel cell in the mid-troposphere, whereas near the surface this forcing term contributes positively (Fig. 9d).

For $\tilde{g} = 0.5$, the pattern of the diabatic heating rate as well as the

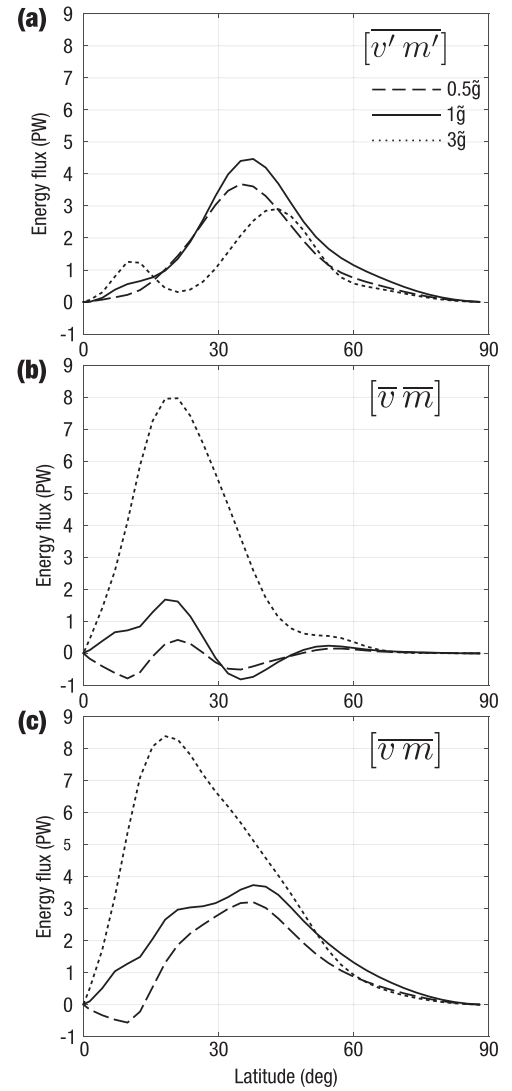


Fig. 5. The poleward moist static energy flux: (a) eddy, (b) mean, and (c) the total contribution using 10-year climatological annual mean for $\tilde{g} = 0.5, 1, \text{ and } 3$.

patterns of eddy heat and momentum fluxes are similar to the reference simulation (Fig. 8b–d). However, these drivers are weaker. This implies that the thermally direct Hadley cell and thermally indirect Ferrel cell become weaker as well, as shown in Fig. 2. The zonal drag force not only weakens as the other drivers, it also changes its pattern in the upper troposphere. The qualitative consideration for $\tilde{g} = 0.5$ in Eq. (5) shows similar contributions to the meridional circulation of all four terms (Fig. 9a–d).

For $\tilde{g} = 3$, the diabatic heating rate not only changes its strength but also its pattern compared to the reference simulation (Fig. 8b). Radiative heating still dominates at the equator; however, in the upper troposphere at mid-latitudes radiative cooling also dominates the diabatic heating rate. Hence, the primary driver of the thermally direct Hadley cell, the diabatic heating rate at the equator, becomes stronger than in the reference simulation. Consequently, the meridional gradient of $[\overline{J}]$ increases around 10° latitude which causes an enhancement of the overturning. While the diabatic heating rate as well as its meridional contrast between radiative warming and cooling enhances in general, the eddy heat and momentum fluxes weaken (Fig. 8c, d). The zonal drag force also changes both pattern and strength but not near the surface.

The changes of the four drivers lead to corresponding changes of the qualitative consideration of Eq. (5) for the sensitivity experiment $\tilde{g} = 3$.

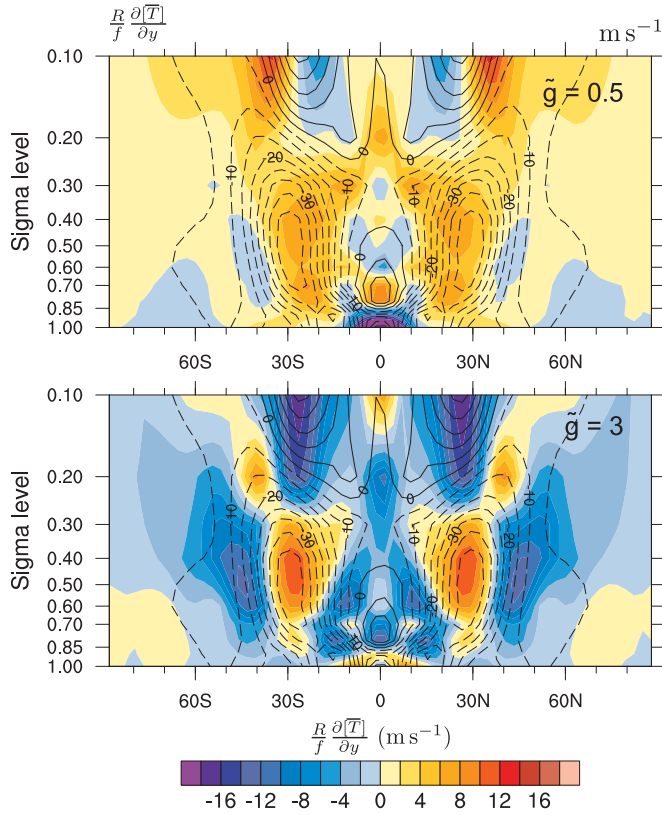


Fig. 6. Thermal wind balance (Eq. (13)): $\frac{R}{f} \frac{\partial \overline{T}}{\partial y}$. Colours indicate the differences (experiment minus reference simulation; unit: m s^{-1}) and contours represent $\tilde{g} = 1$ (contours, interval: 5 m s^{-1}). Shown are the climatological annual means using 10 years.

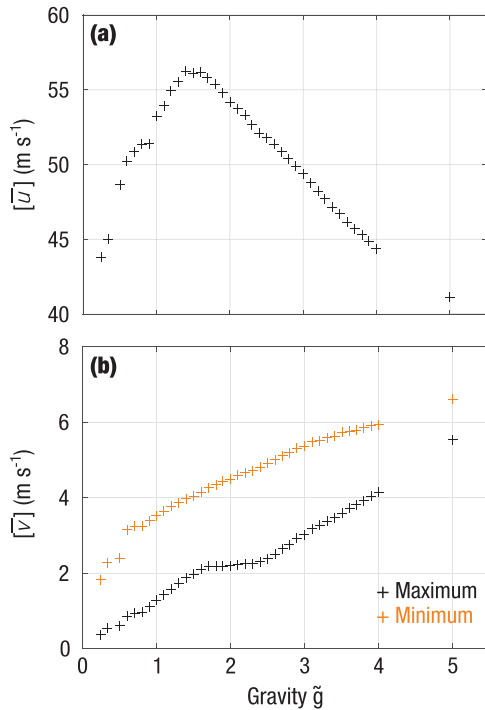


Fig. 7. (a) The maximum of zonal-mean zonal wind as well as (b) the maximum (black) and absolute value of minimum (orange) zonal-mean meridional wind in relation to the gravitational acceleration in the Northern Hemisphere using a 10-year climatological annual mean. (For interpretation of the references to color in this figure legend, the reader is referred to the web version of this article.)

The diabatic heating rate term primarily contributes to the meridional circulation at the equator (Fig. 9a), while both eddy forcing terms are negligible compared to the other forcing terms (Fig. 9b, c). The zonal drag force term becomes the strongest forcing contribution to the meridional circulation (Fig. 9d) of Eq. (5), but the diabatic heating remains the major driver of the Hadley cell, as the meridional circulation of the Hadley cell is responsible for the increase of the zonal drag force. The reason for the latter is that the meridional wind increases with the increase of the Hadley cell. The drag force increases due to its Coriolis force term whereas its eddy momentum contribution (Eq. (11)) becomes negligible for large \tilde{g} (Fig. 9c, d). The zonal drag force acts in the direction of the flow, i.e., westward at the upper troposphere and eastward at the lower troposphere (Fig. 8e). Hence, the pattern of the zonal drag force is dominated by the reversed meridional circulation as a result of the disappearance of the Ferrel cell. James and Grey (1986) showed that an increase in bottom drag increases the mean zonal drag force, which inhibits baroclinic instability. This is consistent with the weakening of the Ferrel cell in our simulations. Finally, the increase of the meridional circulation results in an increase of the zonal drag force.

So far, we discussed the zonal and time mean of the physical processes and the Holton approximation (Eq. (5)) for three cases of \tilde{g} . To deepen the understanding of the underlying physical processes, we consider the behaviour of the physical processes themselves in relation to \tilde{g} .

To examine the diabatic heating rate, its contributions as given in Eq. (10) are examined. The main contribution stems from $c_p \frac{N^2 H}{R} [w]$. Fig. 10a shows the driver associated with diabatic heating as a function of \tilde{g} . The radiative heating at the equator grows with larger \tilde{g} (Fig. 8b). The first term of Eq. (10), $c_p \frac{\partial \overline{T}}{\partial t}$, is negligible because we consider a 10-year annual mean. The third term, $c_p \frac{\partial [v^* w^*]}{\partial y}$, represents the eddy heat flux divergence and is also negligible in the tropics (30°S – 30°N).

Turning back to the dominating term, $c_p \frac{N^2 H}{R} [w]$, Eqs. (6) and (9) suggest $N^2 H \propto g$. The vertical wind speed w decreases with growing \tilde{g} , but the dependence is weak and does not offset the proportionality with \tilde{g} caused by the strong increase of atmospheric stability. Thus, the diabatic heating rate is proportional to \tilde{g} , a result that is primarily caused by the decrease of the atmospheric scale height which is inversely proportional to \tilde{g} . Both diabatic heating and cooling drive the Hadley cell. The minimum (Northern Hemisphere) of the meridional derivative of $[J]$ serves as a measure of the diabatic processes strength (Fig. 10a).

Fig. 10b, c show the maximum eddy heat flux and eddy momentum flux minima and maxima in relation to \tilde{g} . Maximum eddy heat and momentum fluxes are evaluated in the Northern Hemisphere and the minimum eddy momentum flux north of 30°N . Both eddy heat and momentum fluxes show a more complex behaviour related to \tilde{g} with distinct relative maxima/minima that are assumed between $\tilde{g} = 1$ and 2. Branscome (1983) showed that the meridional eddy heat transport depends on static stability. For $\tilde{g} < 1$, the horizontal scale of the eddies increases with N and the eddies become more effective in energy conversion. For strong stratification, i.e., for simulations with $\tilde{g} > 1$, the eddies become shallow and the horizontal scale decreases, thus, in this limit the increase of static stability causes a decrease of the magnitude and vertical scale of the eddy fluxes.

4. Global energy cycle

The global Lorenz energy cycle allows further insights into the equator-to-pole heat transport (Lorenz, 1955). The formalism is given in Appendix D.

Fig. 11 shows the Lorenz energy cycle for $\tilde{g} = 0.5, 1$, and 3 on the aquaplanet. The circles indicate the size of the energy reservoirs and the arrows denote the energy conversions between the reservoirs and the sources and sinks of energy. The values are integrated over the entire

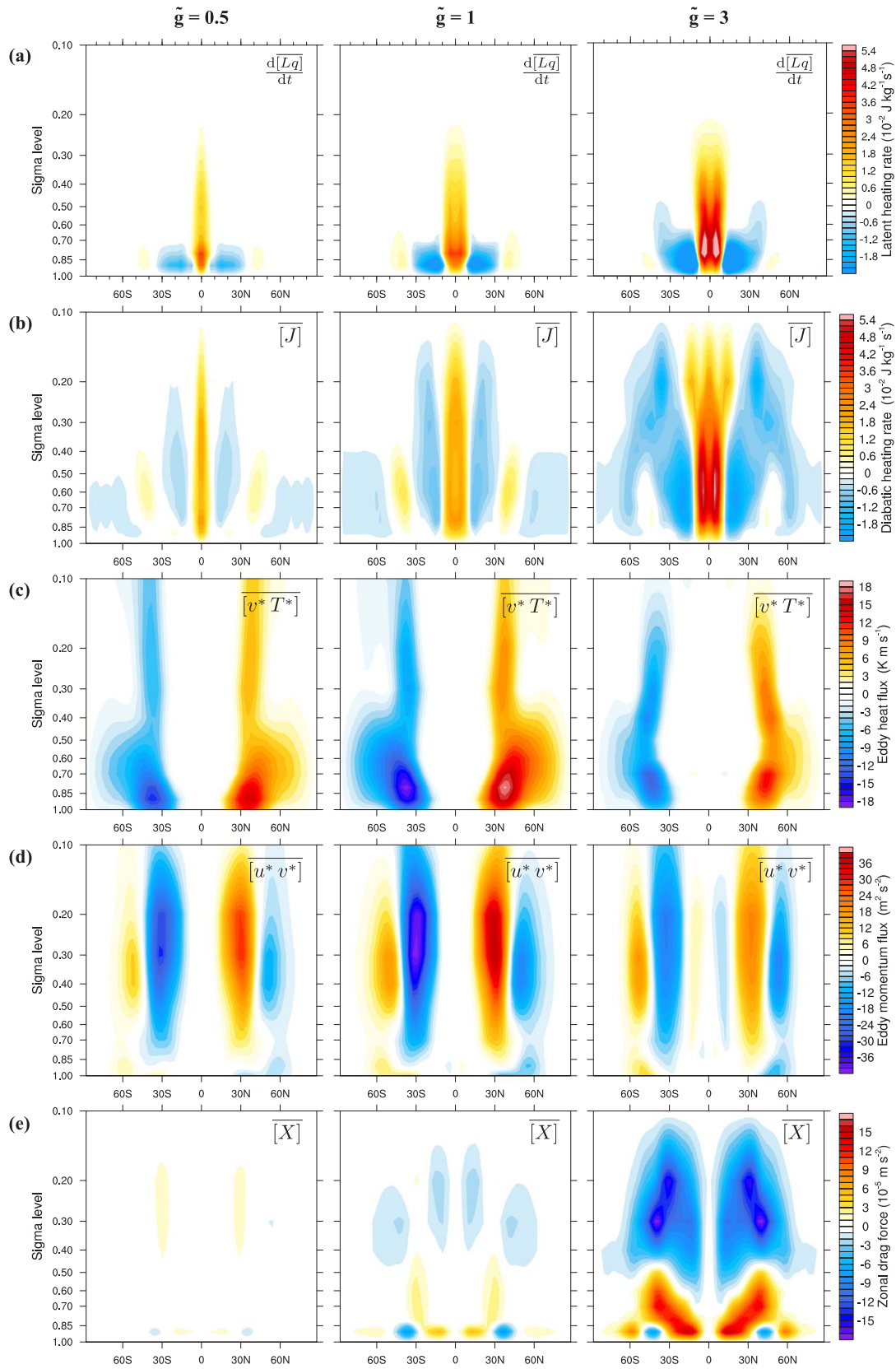


Fig. 8. (a) The latent heating rate and the four drivers of the meridional circulation according to the right-hand side of Eq. (5) as a function of latitude and sigma level for $\tilde{g} = 0.5, 1, \text{ and } 3$: (b) diabatic heating, (c–d) eddy heat and momentum fluxes, and (e) zonal drag force.

atmospheric mass using 10-year climatological annual mean and divided by the planetary surface.

Considering the reference simulation $\tilde{g} = 1$ (Fig. 11), GZ is the only

significant energy source which generates AZ through a net heating at the equator around 15°S–15°N latitude from the surface up to the tropopause (Fig. 8b). Eddy kinetic energy of the circulation is then

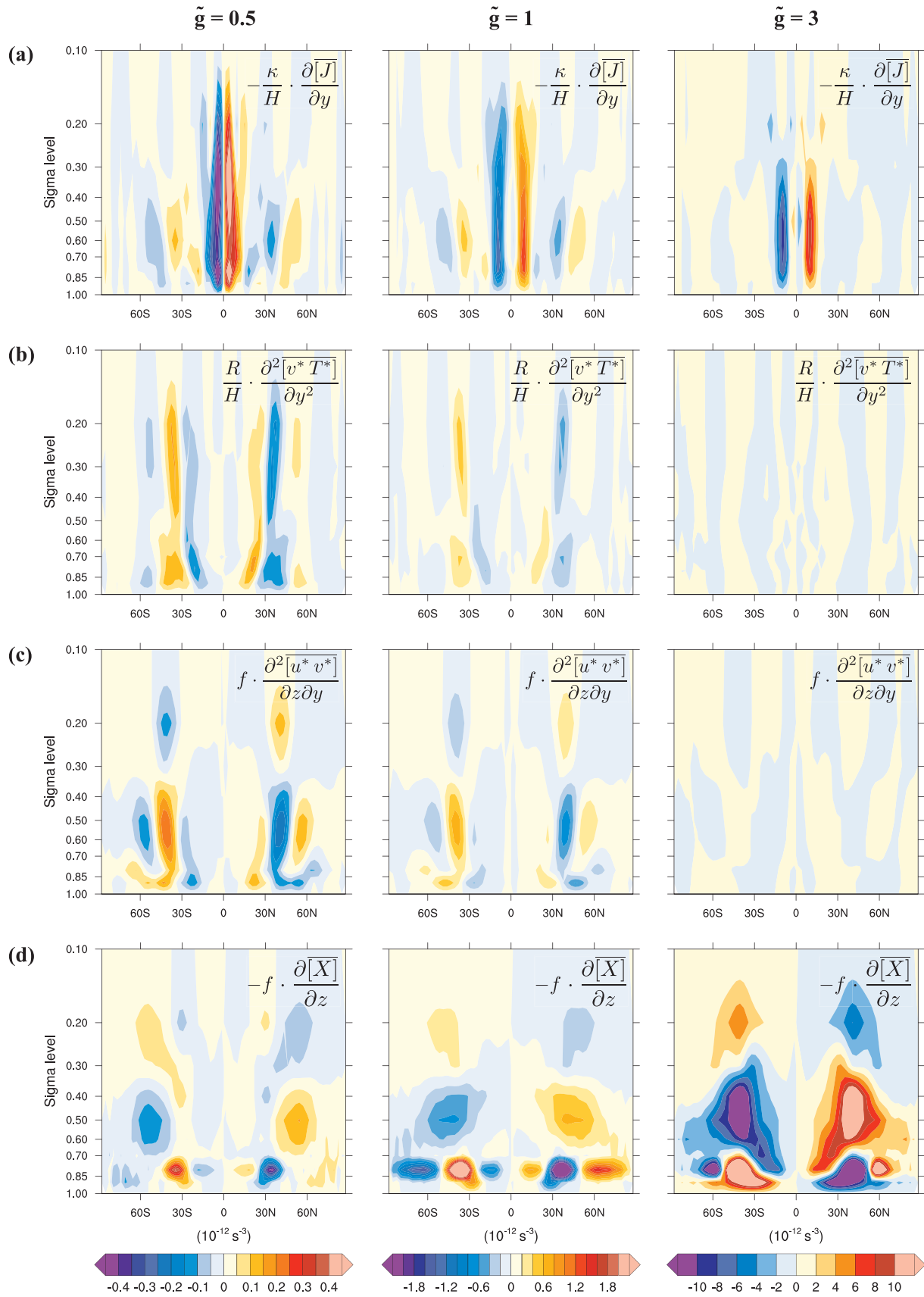


Fig. 9. The four forcing terms of Eq. (5) with positive values indicating positive contributions to the stream function χ (clockwise meridional circulation): (a) diabatic heating, (b–c) eddy heat and momentum fluxes, and (d) zonal drag force, as a function of latitude and sigma level for $\tilde{g} = 0.5, 1$, and 3 . The solid line indicates the zero line. Note that the colour scale of each column has a different maximum magnitude.

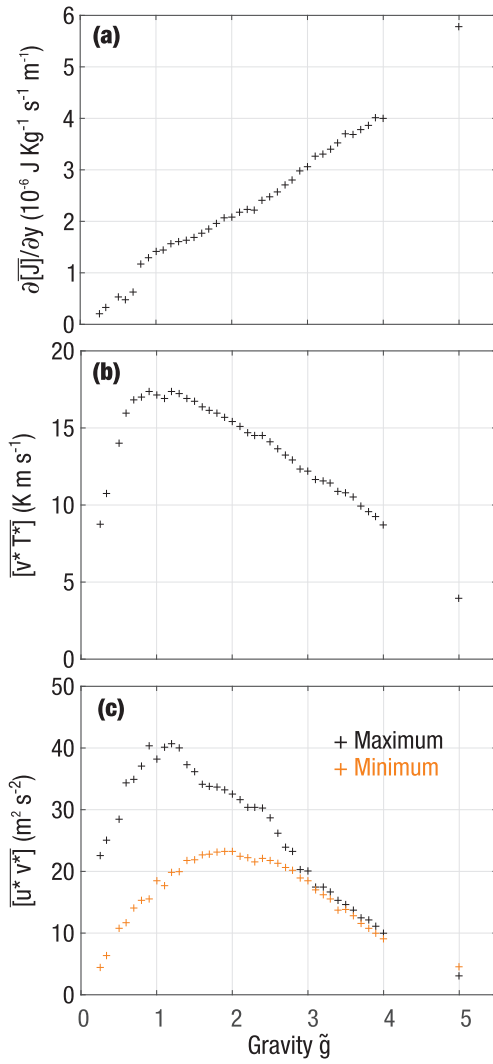


Fig. 10. (a) Minimum of $\frac{\partial \overline{[u^*v^*]}}{\partial y}$ (unit: $10^{-6} \text{ J kg}^{-1} \text{ s}^{-1} \text{ m}^{-1}$) in Northern Hemisphere shown as absolute value, (b) maximum eddy heat flux (unit: K m s^{-1}), and (c) maximum (black) and absolute value of minimum (orange) eddy momentum flux (unit: $\text{m}^2 \text{ s}^{-2}$), as function of gravitational acceleration. (For interpretation of the references to color in this figure legend, the reader is referred to the web version of this article.)

supplied through the baroclinic instability path in the Lorenz cycle, very similar to present-day conditions (Lorenz, 1955; James, 1994). The zonal mean flow KZ is maintained equally by zonal mean conversion CZ and momentum transfer by eddies CK. The transient eddies that are generated by baroclinic instability are also the dominating driver of the Ferrel cell, and together they transport warm air poleward and cold air equatorward in the mid-latitudes (James, 1994):

$$\frac{GZ}{\rightarrow AZ} \xrightarrow{CA} \xrightarrow{AE} \xrightarrow{CE} \xrightarrow{KE} \xrightarrow{DE} \quad (14)$$

The energy cycle and the importance of the baroclinic instability path remain similar in the simulation for $\tilde{g} = 0.5$. Regarding the atmosphere as a heat engine, the efficiency of the atmosphere can be estimated by the ratio of the energy generation by diabatic heating and the mean incoming solar radiation (Peixoto and Oort, 1992) which yields an efficiency of 0.3% for $\tilde{g} = 0.5$ and 0.7% for $\tilde{g} = 1$. Hence, for small \tilde{g} the atmosphere is a less efficient heat engine which explains why the energy reservoirs and conversions decrease compared to $\tilde{g} = 1$ (Fig. 11).

The change from a three-cell to a one-cell circulation is also evident in the energy cycle. For $\tilde{g} = 3$, the energy flow path changes radically, in that the zonal mean conversion, characteristic of the Hadley cell, becomes dominant (Fig. 11). The baroclinic disturbance weakens compared to the reference simulation $\tilde{g} = 1$ leading to a weaker conversion CA illustrating the weakening of the Ferrel cell. GZ strengthens from $\tilde{g} = 1$ to 3 by a factor 2.8; with $\tilde{g} = 3$, GE also generates energy contrary to the simulation with $\tilde{g} = 1$. Since the energy generation increases with \tilde{g} , the efficiency of the atmosphere does as well and reaches a value of 2% with $\tilde{g} = 3$. While AZ for $\tilde{g} = 3$ significantly increases compared to $\tilde{g} = 1$, the other energy reservoirs decrease. KZ decreases as the zonal-mean zonal wind decreases as well (Figs. 2 and 7a). AE and KE weaken due to the broadening and strengthening of the thermally direct Hadley cell in mid-latitudes.

The energy reservoirs as a function of latitude and sigma level (Fig. 12) provide a novel insight into the vertical distribution of the various forms of energy in the atmosphere. For $\tilde{g} = 0.5$ and 1, AZ appears at the equator at higher levels and at the poles at lower levels (Fig. 12a) and is by far the largest energy reservoir. KZ is the second largest reservoir and its location coincides with the subtropical jet stream (Fig. 12b). The small reservoirs associated with the eddies are at lower levels in the polar areas (AE), and assume a maximum at the jet stream maximum (KE).

For $\tilde{g} = 3$, the zonal mean distribution of all energy reservoirs remains similar to the reference simulation. However, AZ only becomes stronger at the poles (50–90° latitude), while it does not change at the

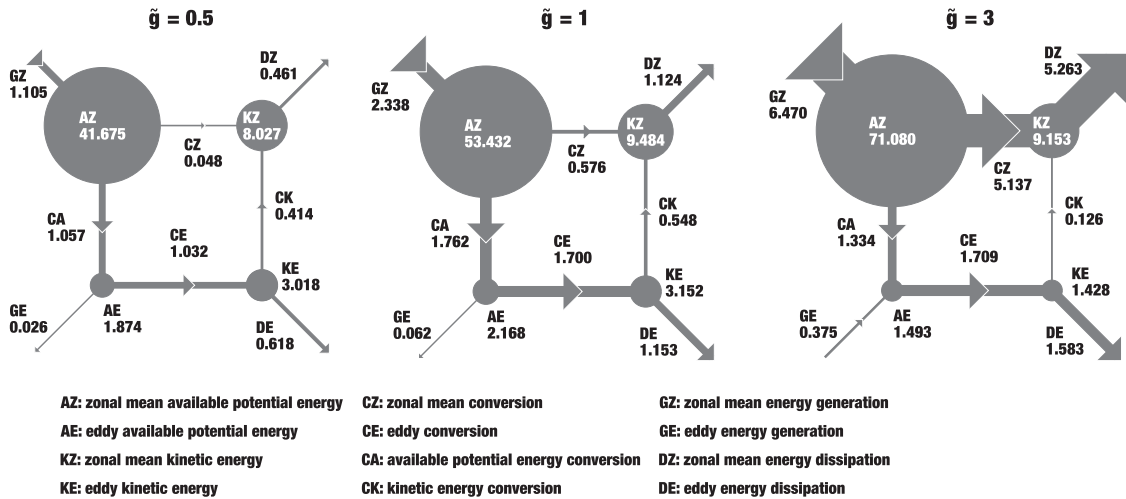


Fig. 11. Lorenz energy cycle using 10-year climatological annual mean for $\tilde{g} = 0.5, 1$, and 3. Arrows indicate orientation of conversions (unit: W m^{-2}) and circles represent energy reservoirs (unit: 10^5 J m^{-2}). The area of the energy reservoir circles and the width of the conversion bars scale with their values. The values are rounded and accurate to three decimal places.

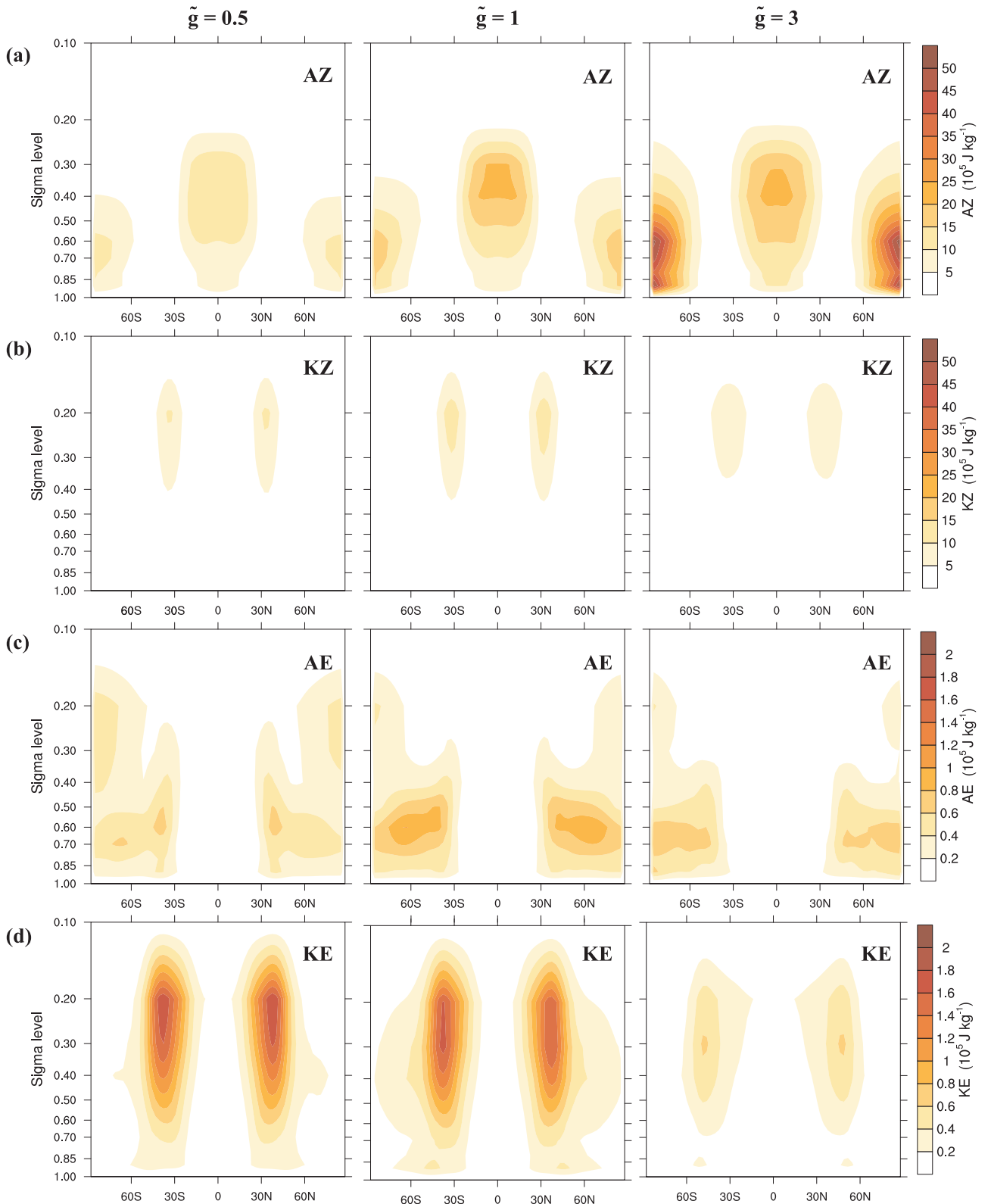


Fig. 12. The four energy reservoirs of the Lorenz energy cycle: (a) zonal mean available potential energy AZ, (b) zonal mean kinetic energy KZ, (c) eddy available potential energy AE, and (d) eddy kinetic energy KE, as a function of latitude and sigma level for $\tilde{g} = 0.5, 1,$ and 3 . Note that the colour scales of zonal mean and eddy energy have different maximum magnitudes.

equator (Fig. 12a–d). Reasons for this behaviour are different temperature changes at the equator and in polar regions for $\tilde{g} = 3$ compared to the reference simulation (Fig. 4).

To further illustrate the connection of the general circulation presented in Section 3 and the Lorenz energy cycle, we analyse the

dependence of each energy conversion on \tilde{g} (Fig. 13). With growing \tilde{g} the radiative heating increases at the equator which contributes mainly to the increase of the direct zonal mean conversion CZ (Fig. 13a). This is the main driver of the thermally direct Hadley cell as discussed in Section 3.2. The conversions CA and CE (Fig. 13c, d) related to the

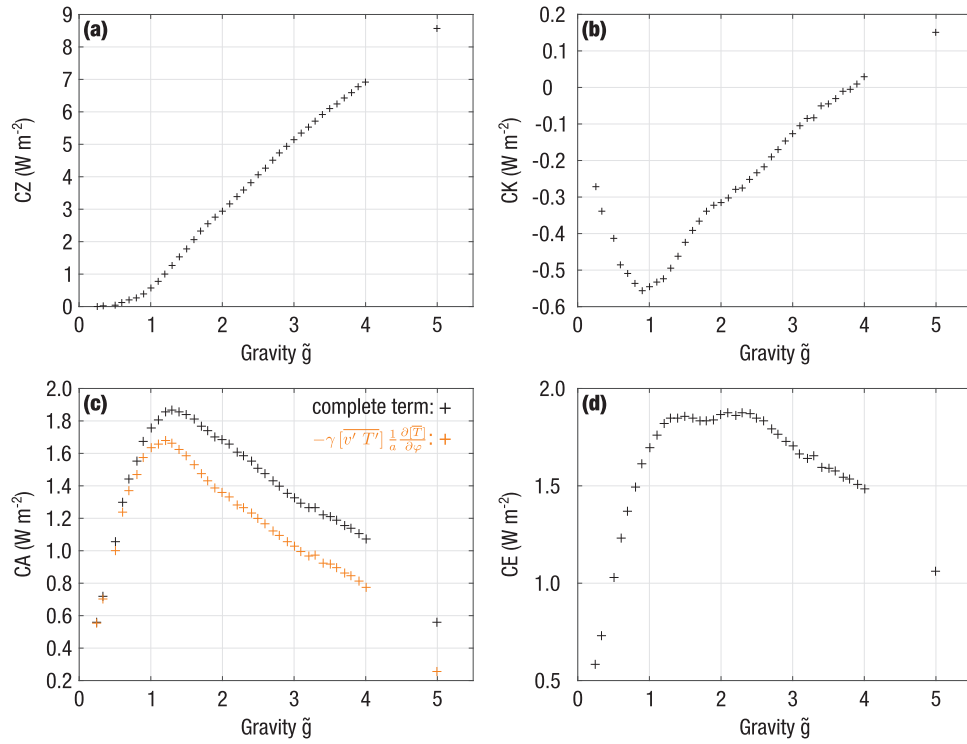


Fig. 13. The energy conversions in relation to gravitational acceleration: (a) direct zonal mean conversion CZ between zonal mean available potential energy and zonal mean kinetic energy, (b) barotropic conversion CK between zonal mean kinetic energy and eddy kinetic energy, (c) baroclinically unstable conversion CA between zonal mean available potential energy and eddy available potential energy and the dominate term $-\gamma[\overline{v'T'}] \frac{1}{a} \frac{\partial \overline{T}}{\partial \varphi}$, and (d) baroclinically unstable conversion CE between eddy available potential energy and eddy kinetic energy.

baroclinic instability show a behaviour that is closely linked to the strength of the Ferrel cell (Fig. 3b). The connection is given as CA is dominated by the term $-\gamma[\overline{v'T'}] \frac{1}{a} \frac{\partial \overline{T}}{\partial \varphi}$ (see Appendix D) which includes eddy heat fluxes. The relation between CE and \tilde{g} shows a broader peak because AE is also fed by GE for large \tilde{g} (Fig. 11). Finally, the relation between the conversion CK and \tilde{g} shows a similar behaviour to that of the Ferrel cell and \tilde{g} (Fig. 3b). The reason is that less energy is converted to KE due to the decreased eddy heat and momentum fluxes with increasing \tilde{g} and consequently less KE is available to be converted to KZ.

5. Summary and conclusion

Our study shows how the meridional atmospheric circulation on an aquaplanet strongly depends on the relative gravitational acceleration \tilde{g} , and hence on planetary mean density. The meridional atmospheric circulation supplies the energy to balance the energy deficit at higher latitudes. A three-cell structure maintains the equator-to-pole heat transport in the reference simulation $\tilde{g} = 1$. This three-cell structure dominates the meridional atmospheric circulation up to around $\tilde{g} \approx 1.4$. In the range of $\tilde{g} = 0.5$ –1.4, the three-cell structure and the zonal-mean zonal wind become stronger with increasing \tilde{g} . For larger \tilde{g} , the thermally indirect cell and the zonal-mean zonal wind become weaker, whereas both thermally direct cells strengthen and merge.

To understand the underlying physical process of these structural changes, the drivers of the meridional circulation and the Lorenz energy cycle were examined. The drivers include the diabatic heating rate, the eddy heat flux, the eddy momentum flux, and the zonal drag force.

Diabatic heating rate per unit mass is the main driver of the thermally direct cell and it increases with \tilde{g} . Increasing \tilde{g} enhances the lapse rate and stabilizes the atmosphere. This is also confirmed by the Lorenz energy cycle illustrating the importance of the direct conversion of available potential energy to the zonal flow for large \tilde{g} .

Eddy heat and momentum fluxes are responsible for maintaining the

thermally indirect Ferrel cell. Both processes increase with \tilde{g} but are reduced substantially when the instability path of the Lorenz energy cycle loses importance in comparison to the zonal mean conversion which drives the Hadley cell.

The reason for the different response of the diabatic heating rate (driving the Hadley cell) and the baroclinic eddies (responsible for the Ferrel cell) to \tilde{g} lies in the different influence of the static stability on these drivers. Increasing \tilde{g} reduces H in inverse proportion and linearly increases N^2 , thus, increasing the diabatic heating rate. But increasing N^2 also impacts the structure of the baroclinic eddies, i.e., the horizontal and vertical scale (Branscome, 1983). First, by increasing static stability the horizontal eddy scale increases making them more efficient, then after a peak efficiency, the horizontal and vertical eddy scale decrease making them less efficient again. Further, the amplitude of the subtropical jet and the baroclinic instability path of the Lorenz energy cycle behave similarly in relation to \tilde{g} . The reason is that with decreasing baroclinicity the amplitude of the subtropical jet decreases (Peixoto and Oort, 1992).

Up to $\tilde{g} = 1.4$ our simulations confirm the results in Kaspi and Showman (2015). They also showed an increase in the strength of all atmospheric cells and a poleward extent of the Hadley cell as predicted by Held and Hou (1980). However, applying the parameterisation of Held and Hou (1980) to our simulations significantly underestimates the position of the poleward boundary of the Hadley cell for large \tilde{g} (converge to about 25° latitude). Furthermore, Kaspi and Showman (2015) also confirmed an increase of static stability with \tilde{g} and a cooling of the polar areas; however, our simulations additionally show a warming of the upper troposphere with \tilde{g} . This warming is likely related to the fact that the radiation scheme of our model is more complex, which also takes water vapor feedbacks into account to estimate the optical thickness of the atmosphere. The development from a three- to a one-cell structure in our simulations is not consistent with the results of Kaspi and Showman (2015). However, as the Hadley cell in their simple GCM also extends further poleward with growing \tilde{g} ,

it is reasonable to assume that the one cell structure may eventually emerge at larger \tilde{g} in their simulations.

In the simulations carried out for this study we kept the sea surface temperatures fixed. This simplification should be relaxed in future experiments by using either an atmospheric module coupled to a slab ocean or a fully dynamical ocean. This coupling would permit a response of the sea surface temperatures and eventually ocean circulation to changes in atmospheric circulation. Preliminary experiments with a slab ocean coupled to the atmosphere suggest that the transition from a three-cell to a one-cell structure of the atmospheric meridional circulation remains a robust feature of the response of the atmosphere to increasing \tilde{g} .

In summary the present study shows that not only planetary size and angular velocity, but also the planetary density crucially determines the structure of the atmospheric circulation and the cycling of energy associated with it. By estimating mass and radius of terrestrial

exoplanets, the terrestrial composition of these planets may be characterised (e.g. Dressing et al., 2015). The characterisation of the planetary composition will then allow a better understanding of the structure of the meridional atmospheric circulation on these planets.

Acknowledgements

We gratefully acknowledge support from Gianna Battaglia, Stefan Muthers, Frank Lunkeit, Sarah Eggleston and the many colleagues who have contributed to our understanding of this subject. Thanks are also due to the high performance computing cluster UBELIX of the University of Bern, especially Nico Färber and Michael Rolli. We also acknowledge with thanks editor Rita Schulz and the three anonymous referees for the constructive comments which improved the quality of the manuscript. This work has been funded by the Center for Space and Habitability of the University of Bern.

Appendix A. Notation for zonal and time averages and deviations

Following standard notation for a variable A , we denote time and zonal means as

$$\bar{A}(\lambda, \varphi, p) = \frac{1}{\tau} \int_0^\tau A(\lambda, \varphi, p, t) dt [A(\varphi, p, t)] = \frac{1}{2\pi} \int_0^{2\pi} A(\lambda, \varphi, p, t) d\lambda, \quad (\text{A.1})$$

and the deviations from their mean, respectively

$$A = \bar{A} + A'A = [A] + A^*. \quad (\text{A.2})$$

The global mean at a pressure level p is given by braces:

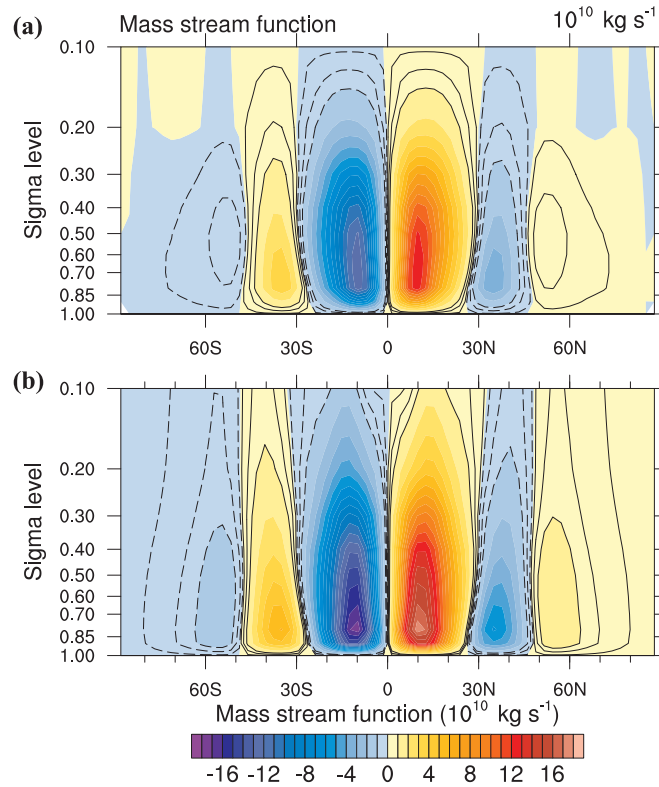


Fig. B.1. Mass stream function shown with colours (interval: $2.5 \cdot 10^{10} \text{ kg s}^{-1}$) and contour lines (for $\pm 0.1 \cdot 10^{10}$, $\pm 0.5 \cdot 10^{10}$, and $\pm 1 \cdot 10^{10} \text{ kg s}^{-1}$): (a) the mass stream function according to Eq. (5), $2\pi \cos(\varphi) [\chi]$, and panel (b) shows the accurate mass stream function given in Eq. (2). Shown are the climatological annual means using 10 years for the reference simulation $\tilde{g} = 1$. Positive values of the stream function indicate clockwise overturning and negative values indicate anti-clockwise overturning (colours, unit: kg s^{-1}).

$$\{A(p, t)\} = \frac{1}{2} \int_{-\frac{\pi}{2}}^{\frac{\pi}{2}} [A(\varphi, p, t)] \cos \varphi d\varphi. \quad (\text{A.3})$$

Appendix B. Holton stream function

To understand the underlying physical process of the general circulation, we examine the specific drivers of the meridional circulation. By considering a β -plane, the meridional circulation can be summarised by one differential equation (Eq. (5)) which is based on the quasi-geostrophic equations for a dry atmosphere. This equation is compared with Eq. (2) by solving the Eq. (5) using successive overrelaxation (SOR, Press et al., 2007). Fig. B.1a shows the mass stream function approximation on a β -plane according Eq. (5) and the accurate solution for the reference simulation $\tilde{g} = 1$. The structure of the circulation is very similar, but the approximation based on Eq. (5) underestimates the strength of the mass stream function. The main reason for the difference is that Eq. (5) does not include latent heating which would be an additional term in Eq. (10). Latent heat release is strong at the equator and latent cooling in the subtropics. Because the pattern is similar to J , latent heating tends to enhance the thermally direct cell. Nevertheless, the structure is correctly represented and, thus, suitable for the examination of the meridional circulation.

Appendix C. Decomposition of the meridional flux

Taking arbitrary variables A and B , the time- and zonal-mean quantities are given by $[\overline{AB}]$, where the two operators are permutable: $[\overline{AB}] = [\overline{BA}]$. The further analysis of $[\overline{AB}]$ by decomposition leads to

$$[\overline{AB}] = [\overline{A}][\overline{B}] + [\overline{A^* B^*}] + [\overline{A' B'}]. \quad (\text{C.1})$$

Taking the northward heat flux as an example to illustrate the meaning of the various terms, we may substitute $A = v$ and $B = T$ leading to the common and useful expansion in observational studies of the general circulation:

$$[\overline{vT}] = [\overline{v}][\overline{T}] + [\overline{v^* T^*}] + [\overline{v' T'}]. \quad (\text{C.2})$$

The total heat flux is decomposed into three different transport terms associated with the mean meridional circulation, stationary eddies, and transient eddies (Peixoto and Oort, 1992). If we take the zonal average first and then take the time average, we get

$$[\overline{AB}] = [\overline{A}][\overline{B}] + [\overline{A'}][\overline{B'}] + [\overline{A^* B^*}]. \quad (\text{C.3})$$

Again taking the northward heat transport as an example, we find

$$[\overline{vT}] = [\overline{v}][\overline{T}] + [\overline{v'}][\overline{T'}] + [\overline{v^* T^*}]. \quad (\text{C.4})$$

As before, the total heat flux is decomposed into three but somewhat different transport terms: the transports by the (steady) mean meridional circulation, the transient mean meridional circulation, and the spatial eddy circulation (Peixoto and Oort, 1992). Since the two operators are permutable, from Eqs. (C.1) and (C.3) follows $[\overline{A}][\overline{B}] = [\overline{A}][\overline{B}]$ and $[\overline{A^* B^*}] + [\overline{A' B'}] = [\overline{A'}][\overline{B'}] + [\overline{A^* B^*}]$. However, on an aquaplanet stationary eddies given by $[\overline{A^* B^*}]$ and (steady) mean meridional circulations given by $[\overline{A'}][\overline{B'}]$ are negligible compared to the remaining contributions of, e.g., the northward heat flux. Thus, on an aquaplanet we have $[\overline{A' B'}] \approx [\overline{A^* B^*}]$.

Appendix D. Lorenz energy cycle

Fig. D.1 schematically shows the energy cycle of the general circulation, where boxes represent energy reservoirs and arrows indicate the direction of conversions corresponding to the definitions below. The Lorenz energy cycle separates eddies into stationary and transient contributions. As the stationary eddy part is negligible on an aquaplanet (Section 2.2), the Lorenz energy reservoir is reduced to four energy reservoirs summarising the contributions of transient and stationary eddies (Eqs. (D.3), (D.7), (D.10), (D.14) and (D.17)).

Here we follow Lorenz (1967) and Ulbrich and Speth (1991).

- c_p : specific heat at constant pressure
- g : gravitational acceleration of the planet
- p : pressure
- a : radius of the planet

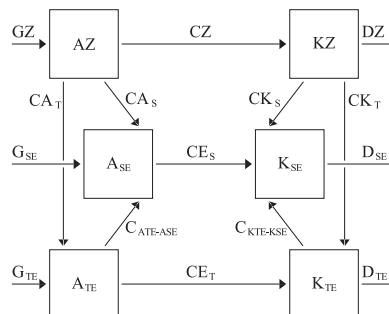


Fig. D.1. Diagram of the global atmospheric energy cycle. Squares represent energy reservoirs and arrows indicate orientation of conversions corresponding to the definitions.

R: gas constant
t: time
T: temperature
T_v: virtual temperature
u: zonal wind
v: meridional wind
 ω : vertical p-velocity
 φ : latitude
 λ : longitude

Stability parameter

$$\gamma = -\frac{R}{p} \left(\frac{\partial}{\partial p} [\bar{T}] - \frac{R}{c_p} \frac{[\bar{T}]}{p} \right)^{-1} \quad (\text{D.1})$$

Zonal mean available potential energy

$$AZ = \frac{\gamma}{2} ([\bar{T}] - \{\bar{T}\})^2 \quad (\text{D.2})$$

Eddy available potential energy

$$AE = A_{SE} + A_{TE} \quad (\text{D.3})$$

Stationary eddy available potential energy

$$A_{SE} = \frac{\gamma}{2} [\overline{T^2}] \quad (\text{D.4})$$

Transient eddy available potential energy

$$A_{TE} = \frac{\gamma}{2} [\overline{T'^2}] \quad (\text{D.5})$$

Zonal mean kinetic energy

$$KZ = \frac{1}{2} ([\bar{u}]^2 + [\bar{v}]^2) \quad (\text{D.6})$$

Eddy kinetic energy

$$KE = K_{SE} + K_{TE} \quad (\text{D.7})$$

Stationary eddy kinetic energy

$$K_{SE} = \frac{1}{2} [\overline{u^2} + \overline{v^2}] \quad (\text{D.8})$$

Transient eddy kinetic energy

$$K_{TE} = \frac{1}{2} [\overline{u'^2} + \overline{v'^2}] \quad (\text{D.9})$$

Conversion from AZ to AE

$$CA = CA_S + CA_T \quad (\text{D.10})$$

Conversion from AZ to A_{SE}

$$CA_S = -\gamma \left([\overline{v^* T^*}] \frac{1}{a} \frac{\partial [\bar{T}]}{\partial \varphi} + [\overline{\omega^* T^*}] \left(\frac{\partial}{\partial p} ([\bar{T}] - \{\bar{T}\}) - \frac{R}{p \cdot c_p} ([\bar{T}] - \{\bar{T}\}) \right) \right) \quad (\text{D.11})$$

Conversion from AZ to A_{TE}

$$CA_T = -\gamma \left([\overline{v' T'}] \frac{1}{a} \frac{\partial [\bar{T}]}{\partial \varphi} + [\overline{\omega' T'}] \left(\frac{\partial}{\partial p} ([\bar{T}] - \{\bar{T}\}) - \frac{R}{p \cdot c_p} ([\bar{T}] - \{\bar{T}\}) \right) \right) \quad (\text{D.12})$$

Conversion from AZ to KZ

$$CZ = -([\bar{u}] - \{\bar{u}\})([\bar{T}_v] - \{\bar{T}_v\}) \frac{R}{p} \quad (\text{D.13})$$

Conversion from AE to KE

$$CE = CE_S + CE_T \quad (\text{D.14})$$

Conversion from A_{SE} to K_{SE}

$$CE_S = -[\overline{\omega^* T_v^*}] \frac{R}{p} \quad (\text{D.15})$$

Conversion from A_{TE} to K_{TE}

$$CE_T = - \left[\overline{\omega' T_v'} \right] \frac{R}{p} \quad (D.16)$$

Conversion from KZ to KE

$$CK = CK_S + CK_T \quad (D.17)$$

Conversion from KZ to K_{SE}

$$CK_S = - \left(\left[\overline{u^* v^*} \right] \frac{1}{a} \frac{\partial [\overline{u}]}{\partial \varphi} + \left[\overline{u^* v^*} \right] \cdot [\overline{u}] \frac{\tan(\varphi)}{a} + \left[\overline{v^* v^*} \right] \frac{1}{a} \frac{\partial [\overline{v}]}{\partial \varphi} - \left[\overline{u^* u^*} \right] \cdot [\overline{v}] \frac{\tan(\varphi)}{a} + \left[\overline{\omega^* u^*} \right] \frac{\partial [\overline{u}]}{\partial p} + \left[\overline{\omega^* v^*} \right] \frac{\partial [\overline{v}]}{\partial p} \right) \quad (D.18)$$

Conversion from KZ to K_{TE}

$$CK_T = - \left(\left[\overline{u' v'} \right] \frac{1}{a} \frac{\partial [\overline{u}]}{\partial \varphi} + \left[\overline{u' v'} \right] \cdot [\overline{u}] \frac{\tan(\varphi)}{a} + \left[\overline{v' v'} \right] \frac{1}{a} \frac{\partial [\overline{v}]}{\partial \varphi} - \left[\overline{u' u'} \right] \cdot [\overline{v}] \frac{\tan(\varphi)}{a} + \left[\overline{\omega' u'} \right] \frac{\partial [\overline{u}]}{\partial p} + \left[\overline{\omega' v'} \right] \frac{\partial [\overline{v}]}{\partial p} \right) \quad (D.19)$$

Conversion from A_{TE} to A_{SE}

$$C_{ATE-ASE} = - \gamma \left(\overline{u' T'^*} \frac{1}{\cos(\varphi)} \frac{\partial \overline{T^*}}{\partial \lambda} + \overline{v' T'^*} \frac{1}{a} \frac{\partial \overline{T^*}}{\partial \varphi} \right) \quad (D.20)$$

Conversion from K_{TE} to K_{SE}

$$C_{KTE-KSE} = - \left(\overline{u' u'^*} \frac{1}{\cos(\varphi)} \frac{\partial \overline{u^*}}{\partial \lambda} + \overline{u' v'^*} \frac{1}{a} \frac{\partial \overline{u^*}}{\partial \varphi} + \overline{u' v'^*} \cdot \overline{u^*} \frac{\tan(\varphi)}{a} + \overline{v' v'^*} \frac{1}{a} \frac{\partial \overline{v^*}}{\partial \varphi} - \overline{u' u'^*} \cdot \overline{v^*} \frac{\tan(\varphi)}{a} + \overline{u' v'^*} \frac{1}{\cos(\varphi)} \frac{\partial \overline{v^*}}{\partial \lambda} \right) \quad (D.21)$$

Budget equations:

$$\frac{\partial AZ}{\partial t} = GZ - CA_S - CA_T - CZ \quad (D.22)$$

$$\frac{\partial ASE}{\partial t} = G_{SE} + CA_S - CE_S + C_{ATE-ASE} \quad (D.23)$$

$$\frac{\partial ATE}{\partial t} = G_{TE} + CA_T - CE_T - C_{ATE-ASE} \quad (D.24)$$

$$\frac{\partial K_{TE}}{\partial t} = - D_{TE} + CE_T + CK_T - C_{KTE-KSE} \quad (D.25)$$

$$\frac{\partial K_{SE}}{\partial t} = - D_{SE} + CE_S + CK_S + C_{KTE-KSE} \quad (D.26)$$

$$\frac{\partial KZ}{\partial t} = - DZ - CK_S - CK_T + CZ \quad (D.27)$$

The left-hand side of the budget equations must vanish in the long-term mean if the system is in steady-state. Note that energy generation and dissipation are estimated by a residual calculation using Eqs. (D.22)–(D.26).

References

- Berta, Z.K., Charbonneau, D., Desert, J.M., Kempton, E.M.R., McCullough, P.R., Burke, C.J., Fortney, J.J., Irwin, J., Nutzman, P., Homeier, D., 2012. The flat transmission spectrum of the super-Earth GJ1214b from wide field camera 3 on the hubble space telescope. *Astrophys. J.* 747, 35.
- Boer, G., McFarlane, N., Laprise, R., Henderson, J., Blanchet, J., 1984. The canadian climate centre spectral atmospheric general circulation model. *Atmos. Ocean* 22, 397–429.
- Branscome, L., 1983. A parameterization of transient eddy heat-flux on a beta-plane. *J. Atmos. Sci.* 40, 2508–2521.
- Caballero, R., Pierrehumbert, R.T., Mitchell, J.L., 2008. Axisymmetric, nearly inviscid circulations in non-condensing radiative-convective atmospheres. *Q. J. Roy. Meteor. Soc.* 134, 1269–1285.
- Chemke, R., Kaspi, Y., 2015. The latitudinal dependence of atmospheric jet scales and macroturbulent energy cascades. *J. Atmos. Sci.* 72, 3891–3907.
- Deming, D., Seager, S., Richardson, L.J., Harrington, J., 2005. Infrared radiation from an extrasolar planet. *Nature* 434, 740–743.
- Dressing, C.D., Charbonneau, D., Dumusque, X., Gettel, S., Pepe, F., Cameron, A.C., Latham, D.W., Molinari, E., Udry, S., Affer, L., Bonomo, A.S., Buchhave, L.A., Cosentino, R., Figueira, P., Fiorenzano, A.F.M., Harutyunyan, A., Haywood, R.D., Johnson, J.A., Lopez-Morales, M., Lovis, C., Malavolta, L., Mayor, M., Micela, G., Motalebi, F., Nascimbeni, V., Phillips, D.F., Piotto, G., Pollacco, D., Queloz, D., Rice, K., Sasselov, D., Segransan, D., Sozzetti, A., Szentgyorgyi, A., Watson, C., 2015. The mass of Kepler-93b and the composition of terrestrial planets. *Astrophys. J.* 800, 135.
- Grose, W.L., Hoskins, B.J., 1979. On the influence of orography on large-scale atmospheric flow. *J. Atmos. Sci.* 36, 223–234.
- Held, I.M., 1978. The vertical scale of an unstable baroclinic wave and its importance for eddy heat flux parameterizations. *J. Atmos. Sci.* 35, 572–576.
- Held, I.M., Hou, A.Y., 1980. Non-linear axially-symmetric circulations in a nearly inviscid atmosphere. *J. Atmos. Sci.* 37, 515–533.
- Held, H.M., 1983. Stationary and quasi-stationary eddies in the extratropical troposphere: theory. In: Hoskins, B., Pearce, R., (Eds.), *Large-scale Dynamical Processes in the Atmosphere*. pp. 127–168.
- Heng, K., Vogt, S.S., 2011. Gliese 581g as a scaled-up version of Earth: atmospheric circulation simulations. *Mon. Not. R. Astron. Soc.* 415, 2145–2157.
- Holton, J.R., 2004. *An Introduction to Dynamic Meteorology*. Third Edition. International Geophysics Series 48, Academic Press, New York, 511 pp.
- Hoskins, B.J., Simmons, A.J., 1975. A multi-layer spectral model and the semi-implicit method. *Q. J. Roy. Meteor. Soc.* 101, 637–655.
- James, I.N., 1994. *Introduction to Circulating Atmospheres*. Cambridge Atmospheric and Space Science Series. Cambridge University Press, Cambridge, 422 pp.
- James, I.N., Gray, L.J., 1986. Concerning the effect of surface drag on the circulation of a baroclinic planetary atmosphere. *Q. J. Roy. Meteor. Soc.* 112, 1231–1250.
- Joshi, M., 2003. Climate model studies of synchronously rotating planets. *Astrobiology* 3, 415–427.
- Joshi, M.M., Haberle, R.M., Reynolds, R.T., 1997. Simulations of the atmospheres of synchronously rotating terrestrial planets orbiting M dwarfs: conditions for atmospheric collapse and the implications for habitability. *Icarus* 129, 450–465.
- Kaspi, Y., Showman, A.P., 2015. Atmospheric dynamics of terrestrial exoplanets over a wide range of orbital and atmospheric parameters. *Astrophys. J.* 804, 60.
- Kreidberg, L., Bean, J.L., Desert, J.M., Benneke, B., Deming, D., Stevenson, K.B., Seager, S., Berta-Thompson, Z., Seifahrt, A., Homeier, D., 2014. Clouds in the atmosphere of the super-Earth exoplanet GJ 1214b. *Nature* 505, 69–72.
- Kuo, H.L., 1965. On formation and intensification of tropical cyclones through latent heat release by cumulus convection. *J. Atmos. Sci.* 22, 40–63.
- Kuo, H.L., 1974. Further studies of the parameterization of the influence of cumulus

- convection on large-scale flow. *J. Atmos. Sci.* 31, 1232–1240.
- Lacis, A.A., Hansen, J., 1974. A parameterization for the absorption of solar radiation in the Earth's atmosphere. *J. Atmos. Sci.* 31, 118–133.
- Laursen, L., Eliassen, E., 1989. On the effects of the damping mechanisms in an atmospheric general circulation model. *Tellus A* 41, 385–400.
- Lewis, S.R., Collins, M., Read, P.L., Forget, F., Hourdin, F., Fournier, R., Hourdin, C., Talagrand, O., Huot, J.P., 1999. A climate database for Mars. *J. Geophys. Res. Planets* 104, 24177–24194.
- Lorenz, E.N., 1955. Available potential energy and the maintenance of the general circulation. *Tellus* 7, 157–167.
- Lorenz, E.N., 1967. *The Nature and Theory of the General Circulation of the Atmosphere*. World Meteorological Organization, Geneva, 161 pp. Reprinted by Bononia University Press 2009.
- Lunkeit, F., Borth, H., Böttinger, M., Fraedrich, K., Jansen, H., Kirk, E., Kleidon, A., Luksch, U., Paiewonsky, P., Schubert, S., Sielmann, S., Wan, H., 2011. *Planet Simulator – Reference Manual Version 16*. Meteorological Institute, University of Hamburg.
- Malbet, F., Lger, A., Shao, M., Goullioud, R., Lagage, P.-O., Brown, A., Cara, C., Durand, G., Eiroa, C., Feautrier, P., Jakobsson, B., Hinglais, E., Kaltenecker, L., Labadie, L., Lagrange, A.-M., Laskar, J., Liseau, R., Lunine, J., Maldonado, J., Mercier, M., Mordasini, C., Queloz, D., Quirrenbach, A., Sozzetti, A., Traub, W., Absil, O., Alibert, Y., Andrei, A., Arenou, F., Beichman, C., Chelli, A., Cockell, C., Duvert, G., Forveille, T., Garcia, P., Hobbs, D., Krone-Martins, A., Lammer, H., Meunier, N., Minardi, S., Moitinho de Almeida, A., Rambaux, N., Raymond, S., Rttgering, H., Sahlmann, J., Schuller, P., Sgransan, D., Selsis, F., Surdej, J., Villaver, E., White, G., Zinnecker, H., 2012. High precision astrometry mission for the detection and characterization of nearby habitable planetary systems with the Nearby Earth Astrometric Telescope (NEAT). *Exp. Astron.* 34, 385–413.
- Manabe, S., Möller, F., 1961. On the radiative equilibrium and heat balance of the atmosphere. *Mon. Weat. Rev.* 89, 503–532.
- Manabe, S., Terpstra, T.B., 1974. The effects of mountains on the general circulation of the atmosphere as identified by numerical experiments. *J. Atmos. Sci.* 31, 3–42.
- Mayor, M., Queloz, D., 1995. A Jupiter-mass companion to a solar-type star. *Nature* 378, 355–359.
- Merlis, T.M., Schneider, T., 2010. Atmospheric dynamics of Earth-like tidally locked aquaplanets. *J. Adv. Model. Earth Sys.* 2, 13.
- Neale, R.B., Hoskins, B.J., 2000. A standard test for AGCMs including their physical parametrizations. I: the proposal. *Atmos. Sci. Lett.* 1, 101–107.
- Peixoto, J.P., Oort, A.H., 1992. *Physics of Climate*. American Institute of Physics, New York.
- Press, W.H., Teukolsky, S.A., Vetterling, W.T., Flannery, B.P., 2007. *Numerical Recipes 3rd Edition: The Art of Scientific Computing*. 3rd Edition. Cambridge University Press, New York, NY, USA.
- Read, P., 2011. Dynamics and circulation regimes of terrestrial planets. *Planet. Space Sci.* 59, 900–914.
- Roeckner, E., Arpe, K., Bengtsson, L., Brinkop, S., Dümenil, L., Esch, M., Kirk, E., Lunkeit, F., Ponater, M., Rockel, B., Sausen, R., Schlese, U., Schubert, S., Windelband, M., 1992. Simulation of the present-day climate with the ECHAM-3 model: impact of model physics and resolution. *Max-Planck Inst. für Meteorol.*, 171, (Report No 93).
- Seager, S., Kuchner, M., Hier-Majumder, C.A., Militzer, B., 2007. Mass-radius relationships for solid exoplanets. *Astrophys. J.* 669, 1279–1297.
- Stephens, G.L., 1978. Radiation profiles in extended water clouds. II: parameterization schemes. *J. Atmos. Sci.* 35, 2123–2132.
- Stephens, G.L., Ackerman, S., Smith, E.A., 1984. A shortwave parameterization revised to improve cloud absorption. *J. Atmos. Sci.* 41, 687–690.
- Svedhem, H., Titov, D.V., Taylor, F.W., Witasse, O., 2007. Venus as a more Earth-like planet. *Nature* 450, 629–632.
- Ulbrich, U., Speth, P., 1991. The global energy cycle of stationary and transient atmospheric waves: results from ECMWF analyses. *Meteorol. Atmos. Phys.* 45, 125–138.
- Watanabe, M., 2005. On the presence of annular variability in an aquaplanet model. *Geophys. Res. Lett.* 32, L05701.
- Williams, G.P., 1988a. The dynamical range of global circulations – I. *Clim. Dyn.* 2, 205–260.
- Williams, G.P., 1988b. The dynamical range of global circulations – II. *Clim. Dyn.* 3, 45–84.
- Williams, G.P., Holloway, J.L., 1982. The range and unity of planetary circulations. *Nature* 297, 295–299.
- Zappa, G., Lucarini, V., Navarra, A., 2011. Baroclinic stationary waves in aquaplanet models. *J. Atmos. Sci.* 68, 1023–1040.